2023 IEEE International Conference on Robotics and Automation (ICRA 2023)
May 29 - June 2, 2023. London, UK

Induced Vertex Motion As a Performance Measure for Surgery in Confined Spaces

Neel Shihora[1] and Nabil Simaan[1†]

***Abstract*— While in the design phase of a robotic system for the procedures performed in surgical confined spaces or hard-to-reach-deep surgical fields, designers can leverage a systematic method to compare the design alternatives for tele-surgical manipulators quantitatively. Unlike most of the work in the literature, we propose an approach for comparing design alternatives by considering the spurious motions along the length of the manipulator in lieu of existing approaches looking at only the end-effector dexterity measures. We propose a performance measure quantifying these spurious motions while the end-effector executes the application-critical tasks such as suturing and tying a knot. A good manipulator design should yield minimal swept volume along its length portions within the confined space. If informed about these spurious motions, that design would lead to reduced force on the internal organs, reducing the pain and discomfort as well as occurrences of extracorporeal inter-manipulator collisions. To validate the proposed approach, we present two illustrative simulation case studies: (1) two planar rigid link serial robots performing the task of following a desired trajectory and (2) two different architectures of tele-surgical manipulators performing the task of passing a circular suture needle under the fulcrum constraints. The results show the applicability of the proposed performance measure in determining the suitability of a particular design alternative for a given task. Although results are promising, using this measure alone for design optimization may compromise overall device dexterity. Therefore, this measure needs to be incorporated into a weighted optimization framework for robot design.**

***Index Terms*— spurious motion, performance measure, confined space, deep surgical fields**

I. Introduction

Emerging surgical paradigms for natural orifice, single-port, and endoluminal access demand dexterous robots for constrained environments. Such robots often have access constraints and a key question during their design stage is how to objectively quantify the suitability of a particular design alternative for a given task. Figure 1 shows snapshots of two planar robots following a circular 2D path. Traces of the paths traversed by each joint are also shown. From the standpoint of reach and collision with the workspace, clearly, the robot in Fig. 1(a) is a better candidate than Fig. 1(b) since it exhibits tip maneuverability with a minimal workspace needed to accommodate the shape changes of the robot for the same task. This paper aims to provide the rationale for a new performance measure called the *induced vertex motion* (IVM) index that quantifies the ability of a particular robot design to operate well within a confined space.

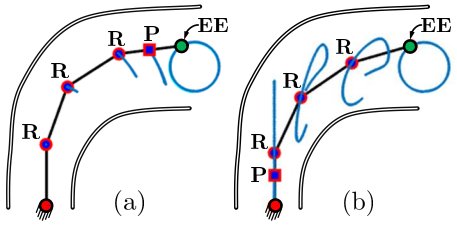

Fig. 1: Two different rigid-link serial robots, (a) of type RRRP and (b) of type PRRR, following a circular path in a confined space. The blue traces show the loci of their joint vertex points

To quantify the shape change of a robot, one can rely on works such as [1] and [2], where the modal representation of a curve fitting along the shape of a serial arm was used to define a shape Jacobian. While the volume of the convex hull of the modal coefficients may be used to quantify the extent of shape change, its relation to the intrinsic kinematics of the robot is not easily understood. Instead, this paper relies on a performance measure definition that captures lateral motions directly and can be more easily understood and used for redundancy resolution and design optimization.

Other relevant works derive from the seminal works of Yoshikawa [3], [4] on kinematic manipulability, works of Angeles on kinematic isotropy [5] and use of the Frobenius norm [6], and the work of Wen 1999 [7] on modeling the kinematic dexterity of constrained robots. These works capture the capabilities of a given robot to impart end-effector twists while disregarding IVM. Within the scope of surgical robotics, a few works considered designs of remote center-of-motion mechanisms to reduce the motion of the extracorporeal portions of surgical robot arms (e.g. [8], [9]). Our contribution is in extending the kinematic analysis to capture the vertex space motion effects of a robot following a path in task space. We define the IVM performance measure and discuss how it can augment kinematic manipulability measures for optimal task-based robot design.

Since our application domain is robotic minimally invasive surgery (MIS), we choose the task of passing a circular needle using a trocar access constraint as one of our benchmarks. In past works by Ding & Simaan [10], [11], it was shown that specific continuum robot designs (e.g. robots that roll about their backbone or use a distal roll wrist) are kinematically better suited for completing this

† Corresponding author
[1]Department of Mechanical Engineering, Vanderbilt University, Nashville, TN 37235, USA (neel.shihora, nabil.simaan)@vanderbilt.edu

The authors were supported in part by the National Institute of Health National Eye Institute grant 1R01EY02813 and by Vanderbilt University internal funds

task with minimal shape change. This paper considers how the IVM measure can be used to select wristed designs for trans-cutaneous constrained workspace applications for MIS. Examples of such applications include thoracic or trans-abdominal surgery when attempting partial resection between organs (e.g. top quadrant liver resection).

An earlier work by Cavosuglu et. al. [12] compared design alternatives of wrists with different topologies with the aim of operating within the thoracic cavity. They posed the need for quantitative comparisons of different manipulator designs in terms of suitability to a given application based on end effector workspace and dexterity. A good and safer manipulator minimizes the manipulator's overall mechanical motion, or in other words, the spurious motion of the manipulator body, to accomplish the desired motion at the manipulator end-effector [13], [14]. Works by Deutschmann et. al. in [15], [16] posed a similar need for a methodology to evaluate the performance of design alternatives.

The following section presents the rationale and formulation of the IVM index. This index is then evaluated for the two planar serial robots as shown in Fig. 1 without a trocar constraint. The formulation of the constrained kinematics of two wristed MIS robot alternatives is then presented as a precursor for a comparative simulation design study that uses the IVM as a design performance measure.

II. Quantifying Induced Vertex Motion

We define a measure to quantify the suitability of a robot design to operate in a confined space as the induced vertex motion (spurious motion) suffered by the robot shape in order for the end effector to complete a given task (e.g., passing a circular needle). This measure can be used to inform robot designers to compare robot design alternatives in terms of the spurious motion of the extracorporeal and intracorporeal portions of the robot arm. Optimizing the design to improve the IVM would minimize the chances of collisions between the intracorporeal manipulator portion and the surrounding tissue or between extracorporeal portions of adjacent manipulator arms.

The following is a minimal common nomenclature used throughout this paper:

$\{\mathrm{A}\}$	A right-handed frame having $\hat{\mathbf{x}}_a, \hat{\mathbf{y}}_a, \hat{\mathbf{z}}_a$ as its unit vectors and point $\mathbf{a}$ as its origin.
${}^a\mathbf{b}$	vector $\mathbf{b}$ described in frame $\{\mathrm{A}\}$
${}^a\mathbf{R}_b$	A rotation from frame $\{\mathrm{A}\}$ to frame $\{\mathrm{B}\}$ (orientation of $\{\mathrm{B}\}$ relative to $\{\mathrm{A}\}$
$\boldsymbol{\xi}$	A 6-dimensional twist vector with linear velocity preceding angular velocity. This twist is described in a hybrid frame parallel to the world frame and coincident with the end-effector
$\mathbf{J}_{xy}$	a Jacobian matrix that maps velocities such that $\dot{\mathbf{x}} = \mathbf{J}_{xy}\dot{\mathbf{y}}$ where $\dot{(\,)}$ designates time derivative. An exception to this notation is $\mathbf{J}_{\xi y}$ such that $\boldsymbol{\xi} = \mathbf{J}_{\xi y}\dot{\mathbf{y}}$
${}^z\boldsymbol{\mathcal{A}}_{xy}$	an adjoint matrix transforming a twist due to a parallel translation of the frame from point ${}^z\mathbf{x}$ to point ${}^z\mathbf{y}$. ${}^z\boldsymbol{\mathcal{A}}_{xy} \triangleq \begin{bmatrix} \mathbf{I} & [{}^z\mathbf{x} - {}^z\mathbf{y}]^\wedge \\ \mathbf{0} & \mathbf{I} \end{bmatrix}$ where $[\cdot]^\wedge$ designates the cross-product matrix form of a vector and $\mathbf{I}$ denotes the 3×3 identity matrix.
$\mathbf{q}$	a joint space vector parameterizing the direct kinematics of the serial arm

Figure 2(a) presents a serial arm with n joints and an end-effector (EE). The robot traversing a task with an EE twist $\boldsymbol{\xi}$ is shown in Fig. 2(b). The induced linear velocities at the vertex points (origins of D-H frames (also center of revolute joints/center of the static portion of a prismatic joint by design) and the end-effector point (EE)) are also shown as $\mathbf{v}_1, \ldots, \mathbf{v}_n$. We denote the base joint (or the vertex point that is static relative to the base of the robot) with an index $i = 0$ and for the case studies presented in this paper, it is considered that $\mathbf{v}_0 = \mathbf{0}$ throughout the task. Also shown are the local planes $\pi_1, \ldots, \pi_n$ perpendicular to each link.

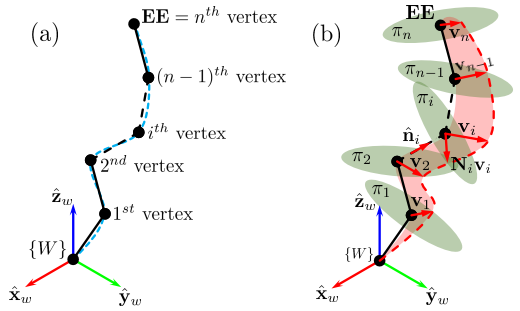

Fig. 2: The nomenclature supporting the derivation of the measure, (a) presents the ordering of the joints for a general serial robot schematic and (b) helps in visualizing the reasoning of the proposed performance metric. The proposed method hypothesize that the good robot should minimize the red shaded area while executing the given end-effector (**EE**) task

In deriving a performance measure that captures this trait for a serial-robot design consisting of n-joints allowing m-DOF, we assume kinematic redundancy, i.e. $m \leq n$ and we define an augmented vertex velocity vector $\breve{\mathbf{v}} \in \mathbb{R}^{3n}$ as:

$$\breve{\mathbf{v}} = \begin{bmatrix} \mathbf{v}_1^{\mathrm{T}} & \mathbf{v}_2^{\mathrm{T}} & \mathbf{v}_3^{\mathrm{T}} & \cdots & \mathbf{v}_n^{\mathrm{T}} \end{bmatrix}^{\mathrm{T}} \tag{1}$$

where, $\mathbf{v}_i$, $i = 1, \ldots, n-1$ denotes the linear velocity of the i^{th} vertex-point of the robot and $\mathbf{v}_n$ is the EE linear velocity (also denoted as $\mathbf{v}_e$). Referring to Fig. 2, the joints are indexed starting from 1 for the very first vertex point that is not static, by design, relative to the base of the robot and n for the end-effector point of the robot. Each joint could allow one or more DOF. Hence, for the generic case, we say that the i^{th} joint of the robot has r_i-DOF and therefore, the DOF of the robot can be defined as $\sum_{i=0}^{n} r_i = m$.

Defining the EE twist as $\boldsymbol{\xi} \triangleq [\mathbf{v}_e^{\mathrm{T}}, \boldsymbol{\omega}_e^{\mathrm{T}}]^{\mathrm{T}}$ where $\mathbf{v}_e$ and $\boldsymbol{\omega}_e$ are the spatial linear and angular velocity of the EE, we can express the instantaneous direct kinematics for a given m-DOF serial-robot as:

$$\boldsymbol{\xi} = \mathbf{J}_{\xi q}\dot{\mathbf{q}} \tag{2}$$

where the first three rows of $\mathbf{J}_{\xi q}$ are the translational Jacobian $\mathbf{J}_v$ such that

$$\mathbf{v}_e = \mathbf{J}_v \dot{\mathbf{q}} \tag{3}$$

The absolute linear velocity of the vertex-points, $\mathbf{v}_i$, can be rewritten as:

$$\underbrace{\begin{bmatrix}\mathbf{v}_1\\ \mathbf{v}_2\\ \vdots\\ \mathbf{v}_n\end{bmatrix}}_{\breve{\mathbf{v}}} = \underbrace{\begin{bmatrix}\mathbf{J}_v{}^{(1/0)} & \mathbf{0} & \dots & \mathbf{0}\\ \mathbf{J}_v{}^{(2/0)} & \mathbf{J}_v{}^{(2/1)} & \dots & \mathbf{0}\\ \vdots & \vdots & \vdots & \vdots\\ \mathbf{J}_v{}^{(n/0)} & \mathbf{J}_v{}^{(n/1)} & \dots & \mathbf{J}_v{}^{(n/n-1)}\end{bmatrix}}_{\breve{\mathbf{J}}} \dot{\mathbf{q}} \tag{4}$$

where, $\mathbf{J}_v^{(i/j)}$ denotes the translational portion of the Jacobian mapping joint space speed of the j^{th} joint ($j = 0$ denotes the base joint and $j = (n-1)$ denotes the last joint of the robot) to the linear velocity of the i^{th} vertex point. The Jacobian $\breve{\mathbf{J}}$ is the joint space to the augmented vertex velocity Jacobian matrix.

To quantify the induced vertex space motion, we relate the EE twist $\boldsymbol{\xi}$ to the induced vertex velocity $\breve{\mathbf{v}}$:

$$\breve{\mathbf{v}} = \breve{\mathbf{J}}\dot{\mathbf{q}} = \underbrace{\breve{\mathbf{J}}\mathbf{J}_v^{+}}_{\mathbf{J}_{\breve{p}x_e}} \mathbf{v}_e = \mathbf{J}_{\breve{p}x_e}\mathbf{v}_e \tag{5}$$

where, $(\cdot)^+$ denotes the Moore-Penrose inverse, a weighted pseudoinverse or a solution of a redundancy resolution strategy, the EE velocity $\mathbf{v}_e = \dot{\mathbf{x}}_e$, and the induced vertex velocities $\breve{\mathbf{v}} = \dot{\breve{\mathbf{p}}}$ with $\breve{\mathbf{p}}$ denoting the augmented vertex point positions.

Noting that the induced vertex velocities that pose a risk of collision with the environment are the velocities in the planes $\pi_1, \dots, \pi_n$, in Fig. 2(b), we define $\mathbf{N}_1, \dots, \mathbf{N}_n$ as the local projection matrices such that $\mathbf{N}_i\mathbf{v}_i$ returns the induced velocity component within π_i where $\mathbf{N}_i$ is given by:

$$\mathbf{N}_i = \mathbf{I} - \hat{\mathbf{t}}_i^{\mathrm{T}}\hat{\mathbf{t}}_i \tag{6}$$

where, $\hat{\mathbf{t}}_i$ denotes the local unit vector tangent of a shape curve describing the serial robot (e.g. a spline) at vertex point i or simply the vector from the proximal to the distal end of link i if one wishes to simplify the computation.

Defining $\breve{\mathbf{N}}$ as a block-diagonal matrix containing $\mathbf{N}_i$, $i = 1..n$, we can express the *lateral induced vertex velocities* $\widetilde{\mathbf{v}} \triangleq \breve{\mathbf{N}}\breve{\mathbf{v}}$. We then use the the vertex space Jacobian in (4) and the instantaneous direct kinematics in (3) to compute:

$$\|\widetilde{\mathbf{v}}\|^2 = \dot{\mathbf{q}}^{\mathrm{T}}\breve{\mathbf{J}}^{\mathrm{T}}\breve{\mathbf{N}}^{\mathrm{T}}\breve{\mathbf{N}}\breve{\mathbf{J}}\dot{\mathbf{q}} = \mathbf{v}_e^{\mathrm{T}}\mathbf{J}_{\breve{p}x_e}^{\mathrm{T}}\breve{\mathbf{N}}^{\mathrm{T}}\breve{\mathbf{N}}\mathbf{J}_{\breve{p}x_e}\mathbf{v}_e \tag{7}$$

A particular design minimizes the norm of the lateral induced vertex velocities if the above quadratic form is minimized. The worst-case lateral induced vertex velocities occur when the commanded EE velocity is along the singular vector of the largest singular value of $\breve{\mathbf{N}}\mathbf{J}_{\breve{p}x_e}$. Since we want a performance measure irrespective of the task $\mathbf{v}_e$, we defined the following two IVM measures:

$$\mathrm{I}_1 \triangleq \sigma_{max}\left(\breve{\mathbf{N}}\mathbf{J}_{\breve{p}x_e}\right), \quad \mathrm{I}_2 \triangleq \prod_{i=1}^{\rho}\sigma_i\left(\breve{\mathbf{N}}\mathbf{J}_{\breve{p}x_e}\right) \tag{8}$$

TABLE I: DH Parameters. Length units are in mm. Angular units are in $radians$

	$\hat{\mathbf{z}}_{i-1}$ to $\hat{\mathbf{z}}_i$		$\hat{\mathbf{x}}_{i-1}$ to $\hat{\mathbf{x}}_i$	
	along $\hat{\mathbf{x}}_i$	about $\hat{\mathbf{x}}_i$	along $\hat{\mathbf{z}}_{i-1}$	about $\hat{\mathbf{z}}_{i-1}$
Joint	$\mathbf{a}_i$	$\boldsymbol{\alpha}_i$	$\mathbf{d}_i$	$\boldsymbol{\theta}_i$
1	0	$\pi/2$	105	q_1
2	500	0	0	q_2
3	0	$\pi/2$	0	q_3
4	0	$-\pi/2$	325	q_4
5	80	$\pi/2$	0	q_5
$6 = p$	0	0	0	q_6
$7 = t$	0	0	q_7	0

where, ρ is the rank of $\breve{\mathbf{N}}\mathbf{J}_{\breve{p}x_e}$. Lower values of I_1 and I_2 denote designs where the induced lateral vertex velocities would be smaller irrespective of the task. While I_1 describes the worst-case scenario, it does not capture the range of variability in the lateral vertex velocities for any task $\mathbf{v}_e$, therefore I_2 is used. Similarly, one may also consider the inverse condition number as an additional measure capturing this variability:

$$\mathrm{I}_3 \triangleq \sigma_{min}\left(\breve{\mathbf{N}}\mathbf{J}_{\breve{p}x_e}\right)/\sigma_{max}\left(\breve{\mathbf{N}}\mathbf{J}_{\breve{p}x_e}\right) \tag{9}$$

The above performance measures are configuration-dependent; therefore, they may be numerically integrated for a given set of benchmarking tasks or workspace to obtain the equivalent of the global conditioning index as in [17].

III. Constrained Kinematics for MIS

Since a key target application for robotic MIS involves trans-cutaneous access through a trocar constraint, we present a constrained kinematics formulation in preparation for the comparative simulation study in section (IV-B). Figure 3 shows a robotic manipulator comprised of a 7-DOF serial arm and a distal dexterity device shown in the form of a continuum segment, but could be replaced with an articulated serial wrist. The serial arm is assumed to have a kinematic architecture inspired by the Kinova Gen3 7DoF robot with a modified link to accommodate the actuation of the tool shaft. Table I provides the D-H table for this serial robot. We define frames $\{P\}$ and $\{T\}$ representing frames at the 6^{th} joint of the serial arm and the frame at the tip of the tool shaft, respectively. Frames $\{P\}$ and $\{T\}$ are parallel and separated by the joint variable q_7. In addition, we define frame $\{G\}$ as the frame at the distal end of the continuum segment and frame $\{E\}$ as the end-effector frame assigned at the distal tip of the gripper.

A. Kinematic formulation nomenclature

As mentioned earlier, we consider that the robotic system is operating under remote center of motion (RCM) constraints (trocar constraints) which resembles a general robot-assisted minimally invasive surgical (RAMIS) setup. Referring to the constrained robotic system in Fig. 3, the presence of an incision point $\tilde{\mathbf{f}}$ applies RCM kinematic constraints on the shaft of the serial arm. We use $\mathbf{f}$ to denote the point that instantaneously coincident with $\tilde{\mathbf{f}}$. The RCM

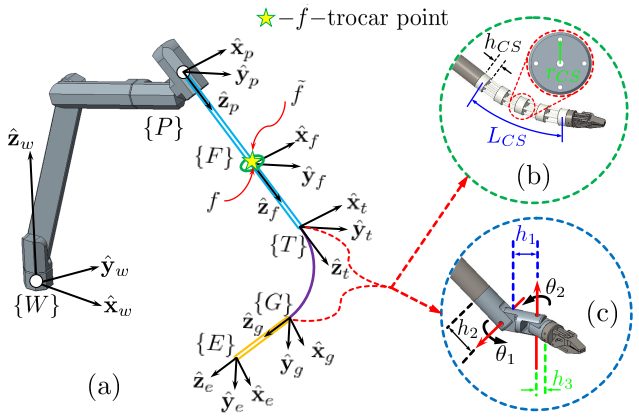

Fig. 3: (a) A 7-DoF serial robot with two distal dexterity alternatives: (b) a continuum robot, (c) an articulated wrist, operating under trocar/fulcrum constraints

constraints at the trocar point $\tilde{\mathbf{f}}$ allow sliding along and rolling about the longitudinal axis of the robot shaft and two tilting motions while preserving the coincidence of the shaft's longitudinal axis with point $\tilde{\mathbf{f}}$.

The RCM constraints demand that the velocity of point $\mathbf{f}$ in a plane perpendicular to the shaft axis $\hat{\mathbf{z}}_t$ should be equal to the velocity of the trocar point $\tilde{\mathbf{f}}$. Defining the linear velocity of the trocar as $\mathbf{v}_{\tilde{f}}$ and the velocity of point $\mathbf{f}$ as $\mathbf{v}_f$, we can express the RCM kinematic constraints as:

$$\mathbf{N}_c \mathbf{v}_f = \mathbf{v}_{\tilde{f}} \quad , \quad \mathbf{N}_c = \mathbf{I} - \hat{\mathbf{z}}_t^{\mathrm{T}} \hat{\mathbf{z}}_t \tag{10}$$

where the matrix $\mathbf{N}_c$ projects the velocity of point $\mathbf{f}$ along a plane perpendicular to the shaft axis. For a trocar fixed in space, $\mathbf{v}_{\tilde{f}} = \mathbf{0}$ is used in equation (10). Otherwise, if $\mathbf{v}_{\tilde{f}}$ is known from a motion tracker, then the robot should follow while maintaining the RCM constraints.

The velocity $\mathbf{v}_f$ is given by the kinematics of the serial arm, while considering point $\mathbf{f}$ as the operational point:

$$\mathbf{v}_f = \mathbf{V}_s \boldsymbol{\mathcal{A}}_{tf} \boldsymbol{\xi}_t \tag{11}$$

where, $\mathbf{V}_s = \begin{bmatrix} \mathbf{I} & | & \mathbf{0} \end{bmatrix}$ is the selection matrix that extracts out the linear velocity from the twist and $\boldsymbol{\mathcal{A}}_{tf}$ is the adjoint twist transformation matrix shifting the operational point from point $\mathbf{t}$ to point $\mathbf{f}$.

Using the serial arm kinematics, $\boldsymbol{\xi}_t = \mathbf{J}_{SA} \dot{\mathbf{q}}$, we can update equation (11) as:

$$\mathbf{v}_f = \mathbf{V}_s \boldsymbol{\mathcal{A}}_{tf} \mathbf{J}_{SA} \dot{\mathbf{q}} \tag{12}$$

Equation (12) and the unconstrained kinematics must be solved simultaneously for the joint speeds of the serial arm and the wrist/continuum segment to satisfy the desired end-effector motion while respecting the trocar constraints. Given the direct kinematics of the distal wrist/continuum segment, the unconstrained kinematics of the system is given by:

$$\boldsymbol{\xi}_e = \mathbf{J}_{\mathbf{x}\tilde{\psi}} \dot{\tilde{\psi}} \tag{13}$$

where, $\tilde{\psi} = [\mathbf{q}^{\mathrm{T}}, \psi^{\mathrm{T}}]^{\mathrm{T}} \in \mathbb{R}^9$ is an augmented configuration space vector parameterizing the direct kinematics of the serial arm and the wrist/continuum segment and ψ is a configuration space vector parameterizing the direct kinematics of the distal wrist or continuum segment. For continuum segment [18], the configuration space vector ψ is defined as $\psi = \begin{bmatrix} \theta_L & \delta \end{bmatrix} \in \mathbb{R}^2$ and is defined as $\psi = \begin{bmatrix} \theta_1 & \theta_2 \end{bmatrix} \in \mathbb{R}^2$ for a 2-DOF wrist like EndoWrist® (as shown in Fig. 3).

For the above definition of $\boldsymbol{\xi}_e$, the Jacobian matrix, $\mathbf{J}_{\mathbf{x}\tilde{\psi}} \in \mathbb{R}^{6\times 9}$, is given by:

$$\mathbf{J}_{\mathbf{x}\tilde{\psi}} = \begin{bmatrix} \boldsymbol{\mathcal{A}}_{te}(\mathbf{J}_{\mathbf{xq}})_{SA} & | & \mathbf{B}_t \, {}^t\boldsymbol{\mathcal{A}}_{ge} \mathbf{J}_{\mathbf{x}\psi} \end{bmatrix} \tag{14}$$

The subscript SA used in equations (12) and (14) indicates that the respective quantity is related to the serial arm. Also, the matrix $\mathbf{B}_t$ is an adjoint relating the twist in frame $\{T\}$ to a frame centered at $\mathbf{t}$ and parallel to the world frame, matrix $\boldsymbol{\mathcal{A}}_{te}$ is an adjoint that considers the end-effector twist induced by the serial arm kinematics, matrix ${}^t\boldsymbol{\mathcal{A}}_{ge}$ is an adjoint that considers the end-effector twist expressed in frame $\{T\}$ induced by the distal device kinematics. These adjoint matrices are given by:

$$\mathbf{B}_t = \begin{bmatrix} {}^w\mathbf{R}_t & \mathbf{0} \\ \mathbf{0} & {}^w\mathbf{R}_t \end{bmatrix} \tag{15}$$

To combine these two linear systems of equations (12) and (13), we use the definition of the augmented configuration space velocity vector $\dot{\tilde{\psi}}$ as defined in the nomenclature. We also define an augmented twist of $\tilde{\boldsymbol{\xi}}_e$ as $\tilde{\boldsymbol{\xi}}_e = \begin{bmatrix} \boldsymbol{\xi}_e^{\mathrm{T}}, & \mathbf{v}_{\tilde{f}}^{\mathrm{T}} \end{bmatrix}^{\mathrm{T}}$. Using these definitions, we can combine equations (12) and (14) into a single linear system of equations defining the constrained instantaneous direct kinematics:

$$\tilde{\boldsymbol{\xi}}_e = \mathbf{J}_{\tilde{\mathbf{x}}\tilde{\psi}} \dot{\tilde{\psi}} \tag{16}$$

where the augmented Jacobian matrix is given by:

$$\mathbf{J}_{\tilde{\mathbf{x}}\tilde{\psi}} = \begin{bmatrix} \boldsymbol{\mathcal{A}}_{te}(\mathbf{J}_{\mathbf{xq}})_{SA} & \mathbf{B}_t \, {}^t\boldsymbol{\mathcal{A}}_{ge} \mathbf{J}_{\mathbf{x}\psi} \\ \mathbf{N}_c \mathbf{V}_s \boldsymbol{\mathcal{A}}_{tf} (\mathbf{J}_{\mathbf{xq}})_{SA} & \mathbf{0} \end{bmatrix} \tag{17}$$

where the first six rows of the Jacobian matrix $\mathbf{J}_{\tilde{\mathbf{x}}\tilde{\psi}}$ capture the unconstrained kinematics of the robotic system and the last three rows capture the constraint equation.

IV. Simulation Case Studies

In this section, we extensively discuss the two simulation case studies (presented in multimedia extension (1)) to validate the applicability of the IVM measures.

A. Planar manipulators without trocar constraint

To illustrate the rationale for this new performance measure, we simulated the two architectures shown in Fig. 1 for the task of following a circular path. The geometric parameters, link lengths, and placement of the prismatic joint relative to the preceding joint were chosen such that both robots initiate the task from the same location.

To illustrate the computation of the Jacobian matrix $\breve{\mathbf{J}}$ as defined in (4), we consider listing the derivation of the vertex point velocity $\mathbf{v}_3$ (3^{rd} vertex point, also the last joint of the robot) for the serial rigid-link planar robot of type PRRR (as shown in Fig. 1(b)) and is given by:

$$\mathbf{v}_3 = \begin{bmatrix} \mathbf{J}_v{}^{(3/0)} & \mathbf{J}_v{}^{(3/1)} & \mathbf{J}_v{}^{(3/2)} & \mathbf{0} \end{bmatrix} \dot{\mathbf{q}} \tag{18}$$

where, Jacobian ${\mathbf{J}_v}^{(3/j)}$, in terms of second coordinate of the Plücker line coordinates, is given by:

$$ {\mathbf{J}_v}^{(3/j)} = \begin{cases} \hat{\mathbf{z}}_j \times (\mathbf{p}_3 - \mathbf{o}_j), & \text{if } j^{th} \text{ joint type = R} \\ \hat{\mathbf{z}}_j, & \text{if } j^{th} \text{ joint type = P} \end{cases} \tag{19} $$

where, $\mathbf{p}_3$ denotes the position vector of the 3^{rd} vertex point and $\mathbf{o}_j$ is the position vector of the j^{th} joint relative to the world frame $\{W\}$.

Figure 4 shows the traces of the performance measures (derived in section (II)) comparing the planar serial architectures of Fig. 1 when performing the given task. Considering the loci of the joint vertices shown in Fig. 1 and the results presented in Fig. 4, it is apparent that the proposed IVM measures can capture the difference between their *induced vertex spaces* (loci of the vertex points).

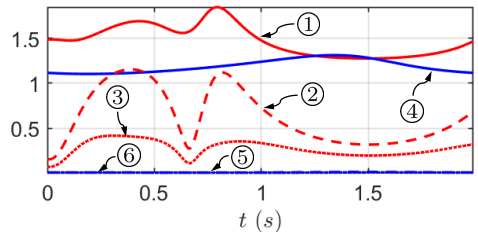

Fig. 4: IVM measures for PRRR architecture (as in Fig. 1); ① values of measure I_1, ② values of measure I_2, ③ values of measure I_3 and IVM measures for RRRP architecture (as in Fig. 1); ④ values of measure I_1, ⑤ values of measure I_2, ⑥ values of measure I_3

B. Spatial manipulators with trocar constraint

We conducted the simulation study to quantitatively compare the different manipulator designs using the proposed measure for their suitability for performing critical surgical tasks within confined spaces, e.g., vitreous and thoracic cavities. We simulated two comparable manipulator architectures (as shown in Fig. 3(b-c)): (1) a serial arm manipulating a continuum segment with a gripper attached to the end disk of the segment and (2) a serial arm manipulating 2-DOF wrist that is kinematically similar to Intuitive Surgical's EndoWrist® instruments. These manipulators were simulated for executing a task of suturing along three straight lines placed in their reachable workspace.

In this task, the insertion and retraction motion of the circular needle was performed at multiple locations along those three straight lines. Considering one such line, the key parameters are represented in Fig. 5. Here, we define a coordinate system $\{N\}$ such that the needle lies in the xy-plane of this frame and the origin of the frame coincides with the center of the circular needle. Also, the unit vector, $\hat{\mathbf{x}}_n$, is defined such that it points to the tip of the needle.

C. Suturing task Nomenclature

$\mathbf{p}_s$ a position vector of the point P_s along the line with respect to the world frame $\{W\}$

L length of the suturing line

s arc length parameter along the suturing curve/line

$\{N\}$ a Cartesian frame whose origin coincides with the center of the circular suture needle and the orientation is given by the rotation of $(-\pi/2)$ about $\hat{\mathbf{z}}_e$

$\{P\}$ a Cartesian coordinate system whose origin coincides with a point $\mathbf{p}_s$ along the suturing line and orientation is given by constraining the $\hat{\mathbf{x}}_p$ tangent to the suturing line and $\hat{\mathbf{y}}_p$ parallel to the x-y plane of the world frame {W}

r radius of the circular suture needle

h a distance from the distal tip of the needle holder to the point where needle is held by the gripper along $\hat{\mathbf{z}}_e$

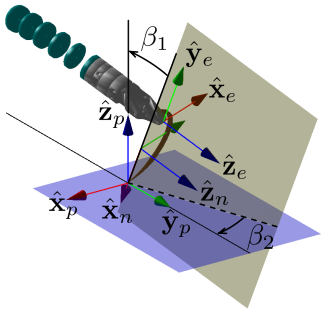

Fig. 5: Nomenclature for the task of suturing at a given point inside the reachable workspace of the robot

D. Task Specification

In this section, specifications for the task of suturing along a line are summarized. For this task, the robot has to insert and retract a circular needle at multiple points along a suturing line specified by two angles α_s and β_s. At a given point $\mathbf{p}_s$ along the suturing line, the end effector frame $\{E\}$ is constrained such that the needle-point passes through an incision point along the suturing line. Given the desired line and needle geometry, the orientation and the position of the end effector are given by:

$$ {}^w\mathbf{R}_e = {}^w\mathbf{R}_n \, e^{-\beta_3 [\hat{\mathbf{z}}]^\wedge} \, {}^e\mathbf{R}_n^{\mathrm{T}} \tag{20} $$

$$ {}^w\mathbf{p}_e = {}^w\mathbf{p}_s + {}^w\mathbf{R}_p \begin{bmatrix} 0 & -h & r \end{bmatrix}^{\mathrm{T}} - r\hat{\mathbf{x}}_n \tag{21} $$

where, the angle $\beta_3 \in [0, \pi/2]$ is measured about $\hat{\mathbf{z}}_n$ and it determines the amount of needle insertion and the rotation matrices ${}^e\mathbf{R}_n$ and $\mathbf{R}_n$ are defined as:

$$ {}^e\mathbf{R}_n = e^{-\frac{\pi}{2}[\hat{\mathbf{z}}_e]^\wedge}, \quad {}^w\mathbf{R}_n = {}^w\mathbf{R}_p \, {}^p\mathbf{R}_n \tag{22} $$

where, the rotation matrix ${}^p\mathbf{R}_n$ is defined by:

$$ {}^p\mathbf{R}_n = e^{\frac{\pi}{2}[\hat{\mathbf{y}}]^\wedge} e^{-\beta_1 [\hat{\mathbf{z}}]^\wedge} e^{-(\frac{\pi}{2}+\beta_2)[\hat{\mathbf{x}}]^\wedge} \tag{23} $$

where, angles β_1 and β_2 are the approach angles that specify the orientation of the suture needle as shown in Fig. 5. The values of the suturing parameters, robot parameters, and the related geometric parameters of the distal wrist and continuum segment are listed in the table II.

Figure 6 presents the plots of IVM measure, I_1, against the normalized simulation time. Similar to the planar case, considering the loci of the joint vertices shown in Fig. 7 and

TABLE II: Suturing parameters used for the task. Here the subscript in denotes the value of the respective quantity when the robot is in its initial configuration. All angular measurements are in $radians$ and all linear measurements are in m.

Suturing Parameters		**Robot Parameters**	
Parameter	**Value**	**Parameter**	**Value**
L	0.045	$(q_1)_{in}$	0
r	0.010875	$(q_2)_{in}$	$2\pi/3$
h	0	$(q_3)_{in}$	$-\pi/4$
β_1	0	$(q_4)_{in}$	0
β_2	0	$(q_5)_{in}$	$-7\pi/30$
$\mathbf{p}_c$	$\mathbf{p}_0 + \begin{bmatrix} 0.015 \\ 0 \\ 0 \end{bmatrix}$	$(q_6)_{in}$	0
		$(q_7)_{in}$	0.3
		$(\psi_1)_{in}$	$\begin{cases} \pi/2, & \text{if } CS \\ 0, & \text{if } EW \end{cases}$
α_s	$-\pi/9$	$(\psi_2)_{in}$	$\begin{cases} 0, & \text{if } CS \\ 0, & \text{if } EW \end{cases}$
β_s	$-\pi/4, 0, \text{and} \pi/4$	$\bar{\mathbf{f}}$	$\mathbf{t} - 0.0513(\hat{\mathbf{z}}_e)_{in}$
Distal dexterous device parameters (Fig. 3)			
Wrist parameters		**Continuum segment parameters**	
Parameter	**Value**	**Parameter**	**Value**
h_1	0.010	L_{CS}	0.025
h_2	0.010	r_{CS}	0.0025
h_3	0.00575	h_{CS}	0.0015

the results presented in Fig. 6, it is apparent that the proposed IVM measures can capture the difference between their *induced vertex spaces* (loci of the vertex points). It should be noted that we mostly rely on the first performance measure I_1 as in (8) for comparison. This measure's average value over the entire task should be lower for better performance in confined spaces.

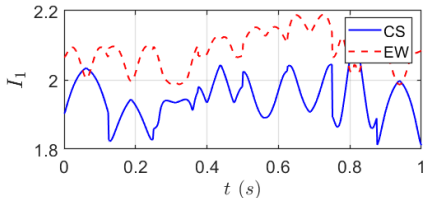

Fig. 6: Values of measure I_1 for the robot architectures shown in Fig. 3. Legend CS refers to the architecture with the continuum segment and EW refers to the architecture with the 2-DOF wrist

V. Conclusions

In this paper, we proposed three new performance measures for serial manipulators that quantify the manipulator's spurious motion while performing a given end-effector task in a confined space. Specifically, we quantified the lateral movements of the joint vertices, which significantly contribute to the change in shape. While working in a confined space, one would choose an architecture that yields the minimum average value of the measure I_1. For a given

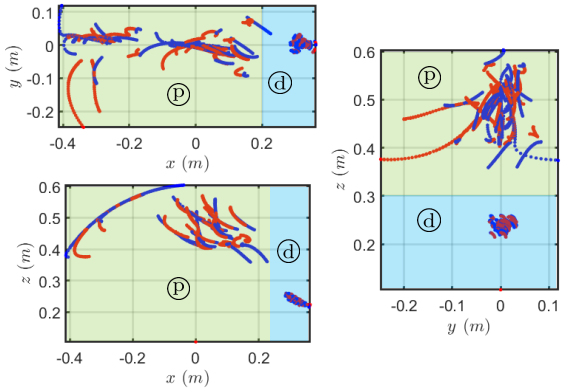

Fig. 7: The blue traces show the loci of joint vertex points of the manipulator equipped with continuum segment and red traces show the loci of joint vertex points of the manipulator equipped with 2-DOF wrist for the suturing task as discussed in this section. These loci show lateral motion, from three different views, of the vertex points which we care about the most for comparing. Shaded areas Ⓟ and ⓓ denote the proximal and distal portions, respectively.

task to be performed in a confined space, a designer can leverage the proposed performance measures to determine the robot's most suitable architecture. Although the results presented in this paper are promising, the measures do not provide insights into what needs to be changed in design for better performance. Also, it is likely that the distal dexterity or overall dexterity of the resulting architecture may not be optimal (e.g. Fig. 8) and there is a need to consider other performance measures such as singularity and kinematic conditioning in a multi-objective optimization paradigm. The measures presented in this paper can also be used to optimize the redundancy resolution strategy and the design parameters of the robot. The IVM measures are fairly dependent on the task, as a particular design appearing suitable for a given task to be performed in a specific portion of the reachable workspace may not be equally ideal for achieving a different or a similar task in another region of the workspace.

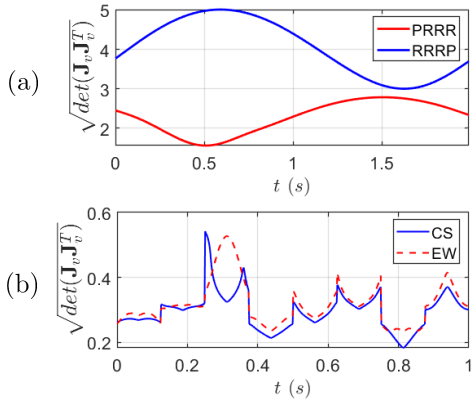

Fig. 8: Transnational manipulability, (a) for the simulation case study presented in section (IV-A) and (b) for the simulation case study presented in section (IV-B)

REFERENCES

[1] H. Mochiyama and H. Kobayashi, "The shape jacobian of a manipulator with hyper degrees of freedom," in *Proceedings 1999 IEEE International Conference on Robotics and Automation (Cat. No.99CH36288C)*, vol. 4, 1999, pp. 2837–2842 vol.4.

[2] H. Mochiyama, E. Shimemura, and H. Kobayashi, "Shape control of manipulators with hyper degrees of freedom," *The International Journal of Robotics Research*, vol. 18, no. 6, pp. 584–600, 1999. [Online]. Available: https://doi.org/10.1177/02783649922066411

[3] T. Yoshikawa, "Manipulability and redundancy control of robotic mechanisms," in *Proceedings. 1985 IEEE International Conference on Robotics and Automation*, vol. 2, 1985, pp. 1004–1009.

[4] ——, "Manipulability of robotic mechanisms," *The International Journal of Robotics Research*, vol. 4, no. 2, pp. 3–9, 1985. [Online]. Available: https://doi.org/10.1177/027836498500400201

[5] J. Angeles and C. S. López-Cajún, "Kinematic isotropy and the conditioning index of serial robotic manipulators," *The International Journal of Robotics Research*, vol. 11, no. 6, pp. 560–571, 1992. [Online]. Available: https://doi.org/10.1177/027836499201100605

[6] W. A. Khan and J. Angeles, "The Kinetostatic Optimization of Robotic Manipulators: The Inverse and the Direct Problems," *Journal of Mechanical Design*, vol. 128, no. 1, pp. 168–178, 08 2005. [Online]. Available: https://doi.org/10.1115/1.2120808

[7] J.-Y. Wen and L. Wilfinger, "Kinematic manipulability of general constrained rigid multibody systems," *IEEE Transactions on Robotics and Automation*, vol. 15, no. 3, pp. 558–567, 1999.

[8] X. Zhou, H. Zhang, M. Feng, J. Zhao, and Y. Fu, "New remote centre of motion mechanism for robot-assisted minimally invasive surgery," *Biomed. Eng. Online*, vol. 17, no. 1, p. 170, Nov. 2018.

[9] C.-H. Kuo, J. S. Dai, and P. Dasgupta, "Kinematic design considerations for minimally invasive surgical robots: an overview," *The International Journal of Medical Robotics and Computer Assisted Surgery*, vol. 8, no. 2, pp. 127–145, 2012. [Online]. Available: https://onlinelibrary.wiley.com/doi/abs/10.1002/rcs.453

[10] J. Ding, K. Xu, R. Goldman, P. Allen, D. Fowler, and N. Simaan, "Design, simulation and evaluation of kinematic alternatives for insertable robotic effectors platforms in single port access surgery," in *2010 IEEE International Conference on Robotics and Automation*, 2010, pp. 1053–1058.

[11] J. Ding and N. Simaan, "Choice of handedness and automated suturing for anthropomorphic dual-arm surgical robots," *Robotica*, vol. 33, no. 8, p. 1775–1793, 2015.

[12] M. Cavusoglu, I. Villanueva, and F. Tendick, "Workspace analysis of robotic manipulators for a teleoperated suturing task," in *Proceedings 2001 IEEE/RSJ International Conference on Intelligent Robots and Systems. Expanding the Societal Role of Robotics in the the Next Millennium (Cat. No.01CH37180)*, vol. 4, 2001, pp. 2234–2239 vol.4.

[13] C.-H. Kuo, J. S. Dai, and P. Dasgupta, "Kinematic design considerations for minimally invasive surgical robots: an overview," *The International Journal of Medical Robotics and Computer Assisted Surgery*, vol. 8, no. 2, pp. 127–145, 2012. [Online]. Available: https://onlinelibrary.wiley.com/doi/abs/10.1002/rcs.453

[14] Y. Chen, S. Zhang, Z. Wu, B. Yang, Q. Luo, and K. Xu, "Review of surgical robotic systems for keyhole and endoscopic procedures: state of the art and perspectives," *Frontiers of Medicine*, vol. 14, no. 4, pp. 382–403, Aug 2020. [Online]. Available: https://doi.org/10.1007/s11684-020-0781-x

[15] B. Deutschmann, R. Konietschke, and C. Ott, "Kinematic analysis of instruments for minimally invasive robotic surgery: Generalization of the reference task," in *New Trends in Medical and Service Robots*, H. Bleuler, M. Bouri, F. Mondada, D. Pisla, A. Rodic, and P. Helmer, Eds. Cham: Springer International Publishing, 2016, pp. 141–152.

[16] B. Deutschmann, R. Konietschke, and A. Albu-Scha¨ffer, "Task-specific evaluation of kinematic designs for instruments in minimally invasive robotic surgery," in *2013 IEEE/RSJ International Conference on Intelligent Robots and Systems*, 2013, pp. 3590–3597.

[17] C. Gosselin and J. Angeles, "A Global Performance Index for the Kinematic Optimization of Robotic Manipulators," *Journal of Mechanical Design*, vol. 113, no. 3, pp. 220–226, 09 1991. [Online]. Available: https://doi.org/10.1115/1.2912772

[18] N. Simaan, "Snake-like units using flexible backbones and actuation redundancy for enhanced miniaturization," in *Proceedings of the 2005 IEEE International Conference on Robotics and Automation*, 2005, pp. 3012–3017.